Research Papers

GREENSUSMATER

Greensusmater
Vol. 3, No. 2, 2026, 11
https://doi.org/10.62755/gsm.2026.11

Check for updates

Effect of Calcination Temperature on Lattice Contraction in Hydrothermally Grown Monoclinic $BiVO_4$ for Photocatalytic Dye Degradation

Alex Triputra Lumban Tobing[1], Rima Nurfitria[1], Rizky Aflaha[2], Quratul Aini[1,*]

[1] *Department of Materials Engineering, Faculty of Industrial Technology, Institut Teknologi Sumatera, Terusan Ryacudu, Way Hui, Jati Agung, Lampung Selatan 35365, Indonesia*
[2] *Department of Physics, Faculty of Mathematics and Natural Sciences, Universitas Gadjah Mada, Sekip Utara PO Box BLS 21, Yogyakarta 55281, Indonesia*

Corresponding author: quratul.aini@mt.itera.ac.id

ARTICLE HISTORY: Received: September 10, 2026 | Revised: October 6, 2026 | Accepted: October 11, 2026

ABSTRACT

Calcination is a routine step in the preparation of $BiVO_4$ photocatalysts, yet its structural effect is often inferred from peak positions alone rather than from full-profile refinement. Here, hydrothermally synthesized $BiVO_4$ was divided into an as-dried portion and portions calcined between 300 and 700 °C, so that calcination temperature was the only variable. The samples were examined by X-ray diffraction with Rietveld refinement, scanning electron microscopy, diffuse reflectance spectroscopy, and photocatalytic degradation of methylene blue (MB) and methyl orange (MO) under 254 nm irradiation. The as-dried powder is already predominantly monoclinic, with a minor zircon-type fraction (below 2 wt%) that disappears between 400 and 500 °C, so the monoclinic structure forms mainly during the hydrothermal step. The unit-cell volume contracts monotonically from 310.179 to 309.750 Å^3, mainly through *b* (0.081%, against 0.035 and 0.023% for *a* and *c*), with no systematic change in the monoclinic angle. The crystallite size stays near 100 nm up to 500 °C and rises to 129 to 158 nm as the particles sinter. The band gap from direct Tauc plots remains between 2.49 and 2.54 eV. Every sample leaves less MB than photolysis alone after 240 min, and the sample calcined at 500 °C gives the highest apparent rate constant, about 2.6 times that of photolysis, whereas MO is not degraded. The MB activity follows neither the lattice contraction nor the band gap, so within the resolution of single runs it is not controlled by the refined structural or optical parameters.

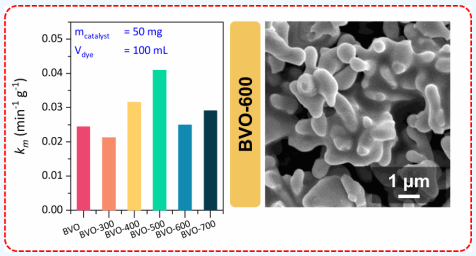

Keywords: *$BiVO_4$; Calcination Temperature; Rietveld Refinement; Lattice Contraction; Photocatalytic Degradation*

1. INTRODUCTION

Synthetic dyes are among the most persistent contaminants discharged by the textile, printing and leather industries [1]. Azo dyes such as methyl orange make up a large share of that discharge, and the azo linkage resists conventional biological treatment. Their colour also reduces light penetration and suppresses photosynthesis in receiving waters. Several azo dyes and the aromatic amines released when they break down are mutagenic [2]. Coagulation and adsorption remove dye from water but transfer it to a solid phase, so the molecule is not destroyed and the loaded sorbent becomes a secondary waste [3]. Advanced oxidation processes instead mineralize the organic structure through reactive oxygen species generated *in situ* [4,5]. Heterogeneous photocatalysis is attractive among these routes because it needs only a semiconductor and a light source at ambient temperature and pressure. Many semiconductors have been examined for this purpose, including TiO_2, ZnO, WO_3, g-C_3N_4 and $BiVO_4$ [6]. TiO_2 and ZnO remain the reference materials, but their band gaps of about 3.2 eV confine absorption to the ultraviolet, which is a small fraction of the solar spectrum.

Monoclinic $BiVO_4$ is a candidate for visible-light operation, with a band gap near 2.4 eV that extends absorption to roughly 520 nm [7,8]. The clinobisvanite polymorph is more active than the tetragonal zircon and scheelite forms, which is attributed to the local distortion imposed by the Bi 6*s* lone pair [9,10]. However, the activity of unmodified $BiVO_4$ is limited by rapid electron-hole recombination and by poor carrier mobility. Calcination is a routine step in the preparation of $BiVO_4$ powders, and the temperature at which it is performed governs crystallinity, defect density and particle morphology [11–13]. An activity optimum at intermediate temperature has been reported, ascribed to a balance between improved crystallinity and loss of surface area [14]. Moreover, calcination is often credited with driving the transformation from a tetragonal precursor to the monoclinic polymorph [9].

These accounts remain difficult to compare, because the structural changes are usually inferred from peak positions and relative intensities rather than from a full-profile refinement. Full-profile refinement has been applied to $BiVO_4$ [15], although not across a calcination series in which the starting powder is already largely monoclinic. A phase transformation, a change in crystallite size and a change in lattice parameters leave different signatures in a diffraction pattern, and separating them requires quantitative refinement across the whole series. Furthermore, when the as-prepared powder is already largely monoclinic, a phase change can account for only a small part of the structural effect of calcination, so the quantity that does respond has to be identified rather than

© 2026 The Authors

This article is licensed under CC-BY 4.0 Open Access

assumed.

In this work, $BiVO_4$ was prepared by a hydrothermal route, and the as-dried powder was divided into portions calcined between 300 and 700 °C so that calcination temperature was the only variable. The six samples were examined by X-ray diffraction with Rietveld refinement of every pattern, by scanning electron microscopy, by diffuse reflectance spectroscopy, and by photocatalytic degradation of methylene blue and methyl orange. The aim is to establish which structural quantities respond to calcination temperature in a powder that is largely monoclinic from the outset.

2. MATERIALS AND METHODS

2.1 Materials

Bismuth nitrate pentahydrate ($Bi(NO_3)_3{\cdot}5H_2O$, ≥98%, Sigma-Aldrich) and ammonium metavanadate (NH_4VO_3, ≥99%, Sigma-Aldrich) were used as the bismuth and vanadium sources. Methylene blue (MB, C.I. 52015, Sigma-Aldrich) and methyl orange (MO, C.I. 13025, Sigma-Aldrich) were employed as model pollutants of opposite ionic character. All reagents were used as received without further purification, and deionized water was used throughout for solution preparation and washing.

2.2 Hydrothermal Synthesis of $BiVO_4$ Nanoparticles

$BiVO_4$ nanoparticles were synthesized by a hydrothermal route following a previously reported protocol [8]. Bismuth nitrate pentahydrate (2.9 g) was dissolved in 50 mL of deionized water under continuous magnetic stirring until a clear solution was obtained. Ammonium metavanadate (0.70 g), corresponding to a Bi:V molar ratio of 1:1, was separately dissolved in 30 mL of deionized water under gentle heating at 60 °C. The vanadium solution was added dropwise to the bismuth solution under continuous stirring, which yielded a yellow suspension that was stirred for a further 30 min at room temperature. The suspension was transferred to a 100 mL Teflon-lined stainless-steel autoclave and held at 150 °C for 24 h. After natural cooling to room temperature, the solid was recovered by vacuum filtration, rinsed thoroughly with deionized water, and dried at 80 °C for 2 h. The as-dried powder was divided into six portions. One portion was retained without thermal treatment and is designated BVO. The remaining five portions were calcined in air for 2 h at 300, 400, 500, 600 and 700 °C at a heating rate of 5 °C min^{-1}, and are designated BVO-300, BVO-400, BVO-500, BVO-600 and BVO-700, respectively, where the numeral denotes the calcination temperature. Calcination temperature was therefore the only variable across the series.

2.3 Materials Characterizations

The crystalline phases were identified by X-ray diffraction (XRD) on a Rigaku SmartLab SE Basic diffractometer with Cu Kα radiation (λ = 1.5406 Å) operated at 40 kV and 50 mA. Patterns were recorded from 5 to 80° 2θ at a step size of 0.01° and a scan rate of 10° min^{-1}, using a 0.5° divergence slit, a 2.5° Soller slit and a Kβ filter. The six patterns were recorded consecutively in a single session with the same instrument alignment. Phase composition, lattice parameters and crystallite size were obtained by Rietveld refinement over 10 to 80° 2θ with Profex 5, which uses the BGMN refinement kernel [16]. The monoclinic clinobisvanite structure (space group I112/b) was taken from COD 9013437, and tetragonal zircon-type $BiVO_4$ (space group $I4_1/amd$) was included as a second phase, with its atomic positions fixed at reported values [17]. The instrumental profile was calculated from the diffractometer geometry, because no line-profile standard was measured on this diffractometer. The refined parameters were the lattice parameters and scale factors of both phases, a specimen-displacement term, the crystallite size of both phases, the microstrain and the preferred orientation of the monoclinic phase, the latter described by sixth-order spherical harmonics, and the background. No internal standard was measured with the diffraction patterns, so the lattice parameters are discussed as relative changes across the series, which share the same instrument, specimen preparation and refinement model. Surface morphology was examined by scanning electron microscopy (SEM) on a JEOL JSM-6510LA instrument operated at 10 kV.

Optical absorption was examined by diffuse reflectance spectroscopy (DRS) on a Shimadzu UV-2600 spectrophotometer equipped with an integrating sphere, using $BaSO_4$ as the reflectance standard. Spectra were recorded over 190 to 800 nm with a slit width of 5 nm and a sampling interval of 0.5 nm. The reflectance R was converted into the Kubelka-Munk function $F(R) = (1 - R)^2/2R$. Band gaps were estimated by extrapolating the linear region of $(F(R)h\nu)^2$ against photon energy to the energy axis, which assumes a direct allowed transition. Monoclinic $BiVO_4$ has an indirect fundamental gap with a direct transition only about 0.2 eV higher [18], and the direct form was used because it is commonly applied to $BiVO_4$ photocatalysts. The indirect form, $(F(R)h\nu)^{1/2}$ extrapolated to the sub-gap baseline, was evaluated for comparison.

2.4 Single Pollutant Degradation Tests

The photocatalytic activity of the six samples was evaluated against MB and MO. In each run, 50 mg of catalyst was suspended in 100 mL of an aqueous dye solution at 5 ppm and irradiated directly, without a dark adsorption step, by four 10 W Philips TUV germicidal lamps ($\lambda \approx 254$ nm) arranged symmetrically around the reaction vessel. Aliquots of approximately 3 mL were collected every 30 min over 240 min and filtered through a syringe membrane filter to remove the catalyst. A no-catalyst control for MB was run under the same irradiation, dye concentration, volume and sampling protocol, on a separate day from the catalyst runs. Absorption spectra were recorded on a Shimadzu UV-1280 spectrophotometer. Because the MB band shifts to shorter wavelength during irradiation, MB was quantified from the integrated absorbance between 550 and 740 nm after subtracting the mean absorbance between 760 and 800 nm, whereas MO was quantified from the absorbance at 464 nm after subtracting the mean absorbance between 700 and 800 nm. The initial dye solution, measured once for each dye on each measurement day, served as the reference, and C/C_0 is the ratio of the integrated band (MB) or of the absorbance at 464 nm (MO) to that of the reference. Apparent rate constants k were obtained from linear fits of $\ln(C_0/C)$ against irradiation time, over 0 to 240 min for MB and over 30 to 240 min for MO, whose absorbance exceeds the initial value at 30 min for several samples, and were divided by the catalyst mass to give the mass-normalised rate constant k_m.

3. RESULTS AND DISCUSSION

3.1 Material and Structural Characteristics of $BiVO_4$ Nanoparticles

Figure 1 shows the surface morphology of the six samples. BVO consists of irregular blocky and short rod-like particles

© 2026 The Authors | CC-BY 4.0

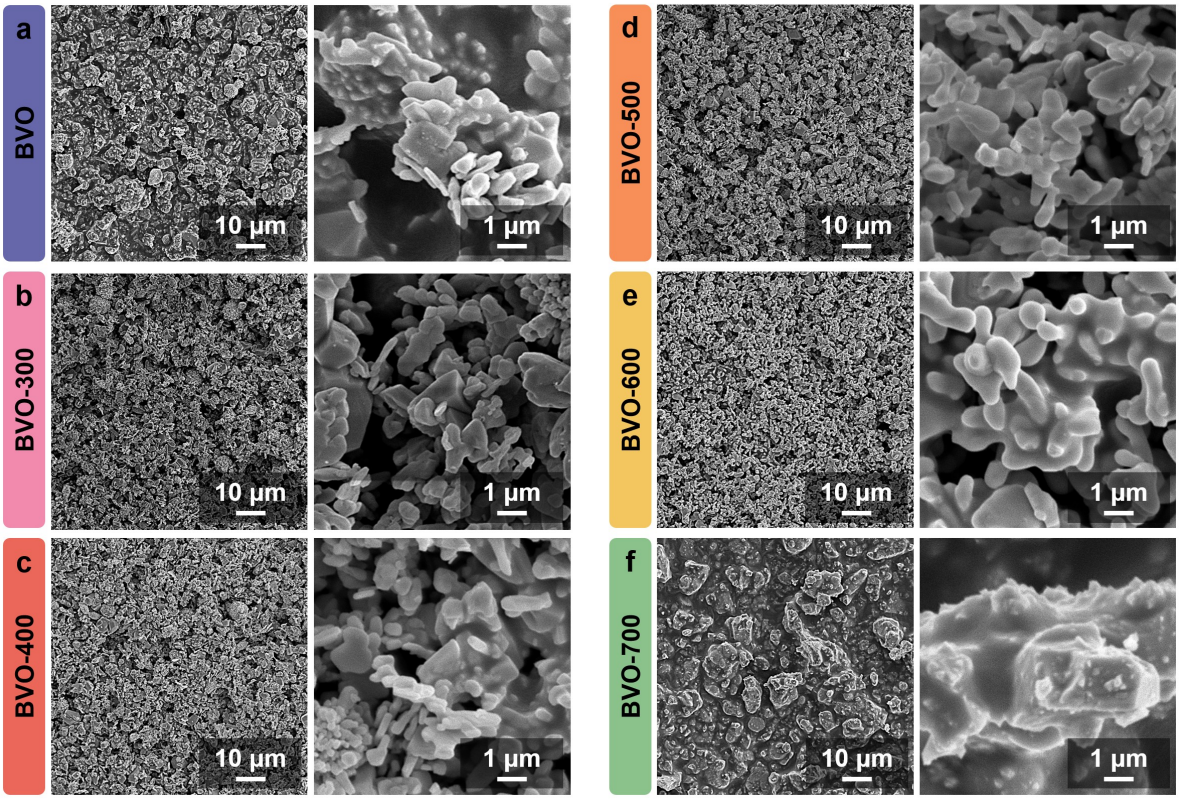

Figure 1. SEM images of (a) BVO, (b) BVO-300, (c) BVO-400, (d) BVO-500, (e) BVO-600 and (f) BVO-700. All scale bars are 1 µm.

with poorly defined edges, accompanied by finer particles below about 200 nm (Figure 1a). The particles range from a few hundred nanometres to about 1 µm across in the fields examined. This blocky and rod-like habit persists in BVO-300 and BVO-400, in which individual particles remain clearly separated (Figure 1b and 1c). From BVO-500 onward the particle outlines become rounded and adjacent particles are joined by necks (Figure 1d and 1e). BVO-700 presents a largely fused surface in which individual particles are no longer resolved and little interparticle porosity is visible (Figure 1f). The progressive rounding and neck formation are consistent with sintering, which becomes appreciable between 500 and 600 °C. Figure 2a presents the X-ray diffraction patterns of the six samples together with the reference pattern of monoclinic $BiVO_4$ (PDF#14-0688). Every strong reflection is indexed to the monoclinic clinobisvanite structure, and the splitting of the (200) and (020) reflections near 34.5 and 35.2° is resolved in all six samples, including the as-dried BVO. However, BVO, BVO-300 and BVO-400 also show two weak reflections at 24.4 and 32.7°, which correspond to the (200) and (112) reflections of tetragonal zircon-type $BiVO_4$ (Figure 2b to 2d). These reflections are absent from BVO-500 onward (Figure 2e to 2g). The monoclinic phase therefore forms mainly during the hydrothermal treatment at 150 °C, and the minor zircon-type fraction disappears between 400 and 500 °C. This is consistent with the transformation of zircon-type $BiVO_4$ into the scheelite structure between 420 and 500 °C, which becomes monoclinic on cooling [17]. No other reflection is observed up to 600 °C. Moreover, weak additional reflections near 26.6, 27.2 and 31.7° appear in BVO-700, which suggests the onset of a minor second phase that the present data do not identify. Because that phase is not included in the refinement, the refined values for BVO-700 carry more uncertainty than those for the other five samples. Rietveld refinements are shown in Figure 2b to 2g, and in each case the calculated profile reproduces the observed intensities across the full angular range, with R_{wp} between 10.6 and 12.7% (Table 1). In BVO, BVO-300 and BVO-400 the zircon-type phase refines to less than 2 wt%. The refined unit-cell volume of the monoclinic phase decreases monotonically from 310.179 $Å^3$ for BVO to 309.750 $Å^3$ for BVO-700, as plotted in Figure 2i. The total change of 0.43 $Å^3$ is more than 30 times the mean standard deviation returned by the refinement, although such standard deviations are known to underestimate the true parameter uncertainty. Moreover, the decrease is already monotonic over the five samples up to 600 °C, so it does not rest on BVO-700 and its unindexed second phase. The contraction amounts to 0.138% and is anisotropic, with b shrinking by 0.081% while a and c shrink by 0.035 and 0.023%, respectively. The ratio b/a is insensitive to zero-point and specimen-displacement errors, because the (200) and (020) reflections that fix it lie only 0.7° apart. It changes by at most 0.03% up to BVO-500 and then falls by about 0.06% at BVO-600, so the b-dominated contraction above 500 °C is not an artefact of an angular error. Meanwhile, the monoclinic angle γ shows no systematic trend across the series, which indicates that the degree of monoclinic distortion is unchanged by calcination. The lattice therefore densifies without a change in symmetry, which is consistent with the progressive removal of defects retained from the hydrothermal synthesis. The crystallite size of the monoclinic phase is plotted in Figure 2h. It remains between 96 and 103 nm from BVO through BVO-500 and then rises to 158 nm for BVO-600 and 129 nm for BVO-700. This step between 500 and 600 °C indicates a threshold for thermally

© 2026 The Authors | CC-BY 4.0

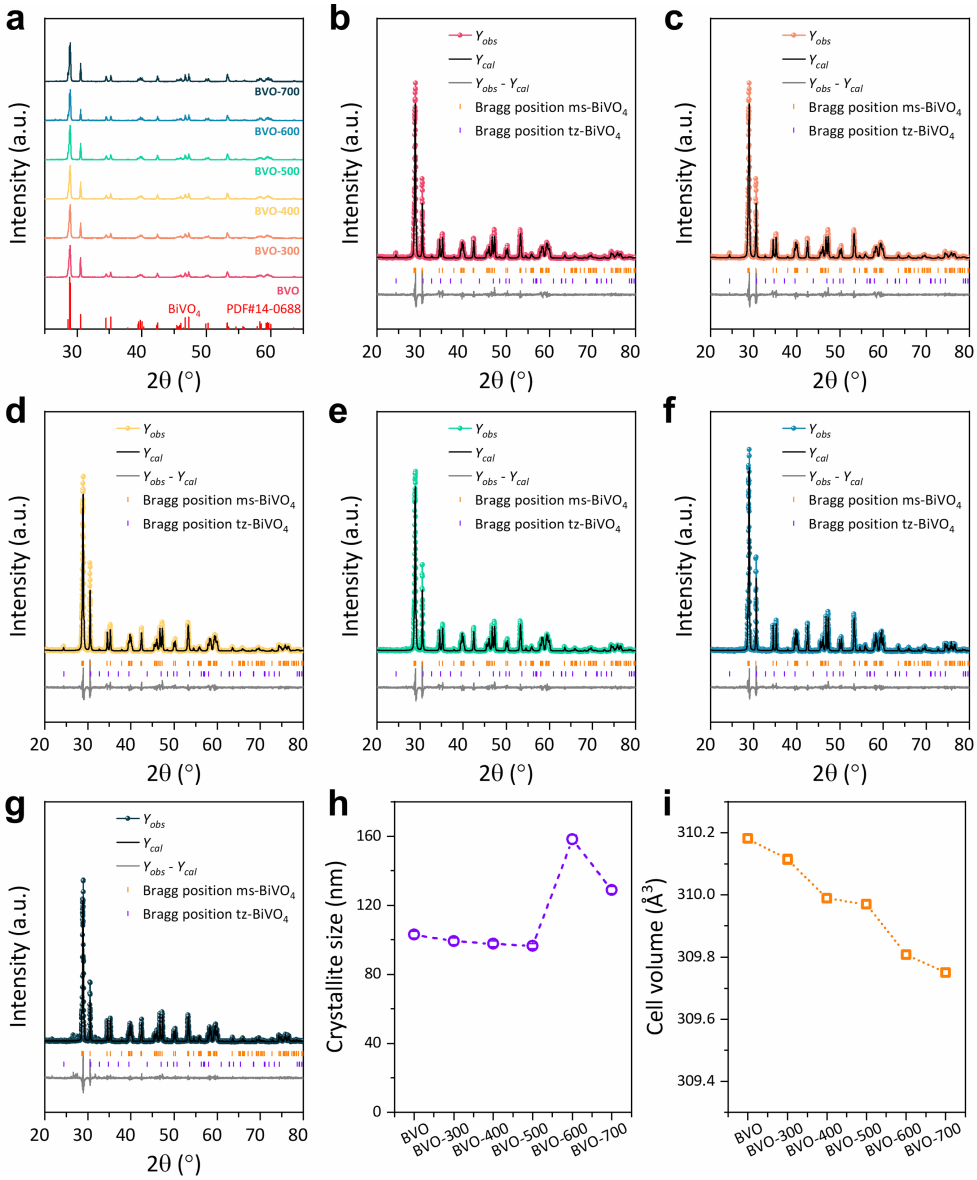

Figure 2. (a) XRD patterns of BVO, BVO-300, BVO-400, BVO-500, BVO-600 and BVO-700, with the reference pattern of monoclinic $BiVO_4$ (PDF#14-0688). Rietveld refinement of (b) BVO, (c) BVO-300, (d) BVO-400, (e) BVO-500, (f) BVO-600 and (g) BVO-700, showing the observed (Y_{obs}) and calculated (Y_{cal}) profiles, their difference, and the Bragg positions of monoclinic scheelite (ms-) and tetragonal zircon-type (tz-) $BiVO_4$. The tz-$BiVO_4$ phase is detected only in (b) to (d), and its Bragg positions in (e) to (g) are shown for comparison. (h) Crystallite size and (i) unit-cell volume of the monoclinic phase; the standard deviations from the refinement are smaller than the symbols.

Table 1. Rietveld refinement results of the six samples (Profex/BGMN). D is the crystallite size and k_2 the BGMN microstrain parameter of the monoclinic phase; n.d., not detected.

Parameter	BVO	BVO-300	BVO-400	BVO-500	BVO-600	BVO-700
a (Å)	5.19705	5.19592	5.19588	5.19589	5.19641	5.19523
b (Å)	5.09843	5.09881	5.09740	5.09703	5.09425	5.09430
c (Å)	11.7066	11.7057	11.7043	11.7045	11.7036	11.7039
γ (°)	90.3797	90.3708	90.3670	90.3600	90.3792	90.3741
V (Å^3)	310.179	310.113	309.988	309.970	309.808	309.750
b/a	0.98102	0.98131	0.98105	0.98097	0.98034	0.98057
D (nm)	103	99	97	96	158	129
k_2 (10^{-6})	1.25	1.29	0.92	0.55	0.18	0.07
Zircon-type (wt%)	1.65	1.62	1.49	n.d.	n.d.	n.d.
R_{wp} (%)	11.9	11.9	11.7	11.5	10.6	12.7

© 2026 The Authors | CC-BY 4.0

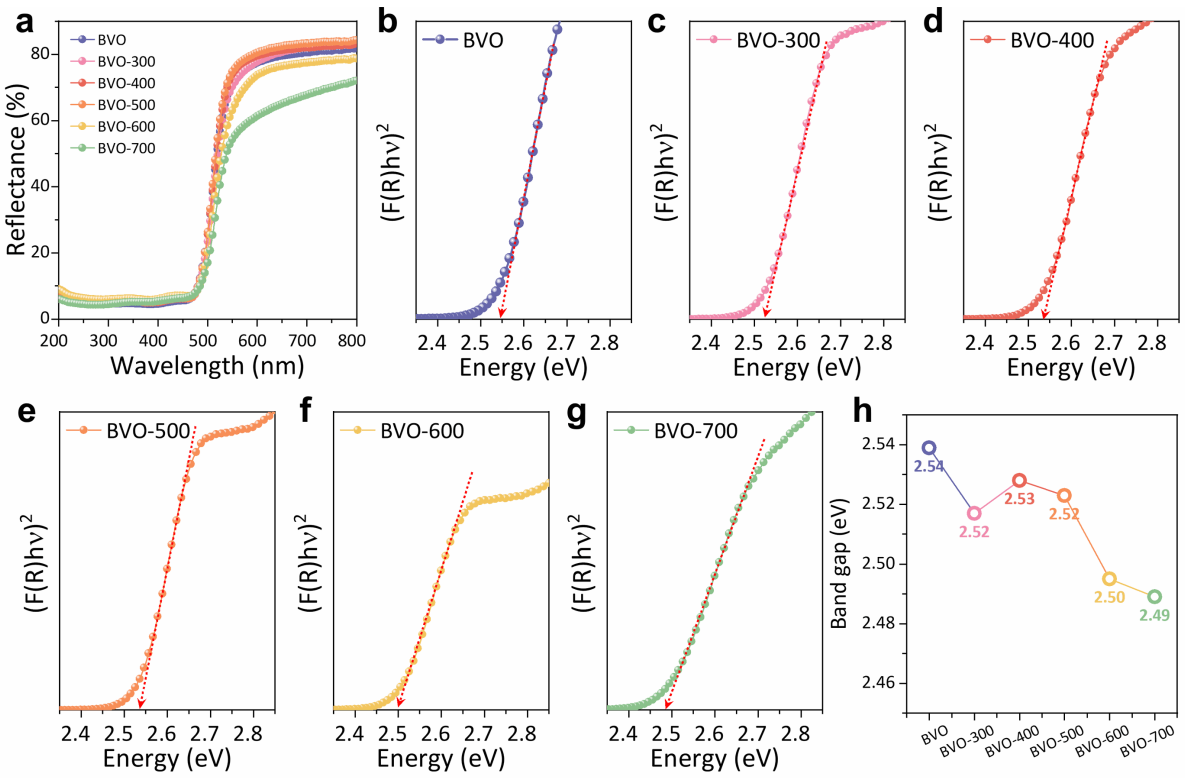

Figure 3. (a) Diffuse reflectance spectra of BVO, BVO-300, BVO-400, BVO-500, BVO-600 and BVO-700. Tauc plots of $(F(R)h\nu)^2$ against photon energy for (b) BVO, (c) BVO-300, (d) BVO-400, (e) BVO-500, (f) BVO-600 and (g) BVO-700, with the linear extrapolation shown as a dotted line. (h) Band gap of each sample.

activated grain growth, and it coincides with the interval in which rounding and neck formation are first seen in Figure 1. Meanwhile, the refined microstrain decreases steadily above 300 °C (Table 1), which is consistent with the defect removal inferred from the lattice contraction. However, the instrumental profile was calculated rather than measured on a standard, and for BVO-600 and BVO-700 the sample broadening is comparable to the instrumental width. Their sizes therefore carry a larger uncertainty than the standard deviations suggest, and the difference between them is not interpreted. The crystallite sizes are smaller than most of the particles seen by SEM, which range from a few hundred nanometres to about 1 µm, so these particles are polycrystalline aggregates rather than single crystals.

Figure 3a shows the diffuse reflectance spectra of the six samples. Every sample reflects weakly below about 470 nm, including at the 254 nm line of the lamps used for the photocatalytic tests, and shows a steep absorption edge near 510 nm. The Tauc plots for a direct allowed transition in Figure 3b to 3g give band gaps of 2.54, 2.52, 2.53, 2.52, 2.50 and 2.49 eV for BVO through BVO-700 (Figure 3h). The band gap is therefore essentially unchanged up to 500 °C, although the cell volume contracts monotonically over the same interval, so the lattice contraction does not measurably shift the absorption onset. The indirect allowed form gives lower values with the same behaviour across the series, so this comparison does not depend on the assumed transition. The two highest temperatures give slightly lower values, and their reflectance above the edge is also lower, most clearly for BVO-700 (Figure 3a), whose Tauc plot extends to lower energy below the edge (Figure 3g). This additional sub-gap absorption is consistent with the minor second phase detected by XRD in BVO-700 and with its fused surface seen by SEM.

3.2 Photocatalytic Degradation of Single Pollutants

Figure 4a shows the removal of MB by the six samples. After 240 min, C/C_0 lies between 0.54 and 0.72, with the lowest value for BVO-500. The linear fits in Figure 4b give apparent rate constants between 1.1 and 2.1 $\times$ 10^{-3} min^{-1}, and the faster decrease during the first 30 min, which for most catalysts includes adsorption of the cationic dye, gives these fits a positive intercept. The mass-normalised rate constants in Figure 4c follow the same order, with the highest value for BVO-500. Part of this removal may arise from direct photolysis at 254 nm. In a no-catalyst control under the same conditions, which is not included in Figure 4, MB decreased by 17% after 180 min and by 22% after 240 min (k = 0.8 $\times$ 10^{-3} min^{-1}). This photolysis level lies within the range reported for MB under four 10 W lamps at 254 nm, from a slight decrease over 240 min [19] to about 33% after 180 min [20], depending on the arrangement of the lamps. Every catalyst ends below the photolysis level after 240 min, but BVO and BVO-300 remain close to it, and the clearest enhancement is obtained with BVO-500, whose rate constant is about 2.6 times that of photolysis. However, the runs were performed once, the control was recorded on a separate day, and BVO-600 and BVO-700 were measured on a different day from the other four samples, so the ranking between neighbouring samples should be read with caution.

In every catalysed run, the absorption maximum of MB shifted to shorter wavelength during irradiation, whereas it remained at its initial position in the control. A shift of this kind is a signature of successive N-demethylation, in

© 2026 The Authors | CC-BY 4.0

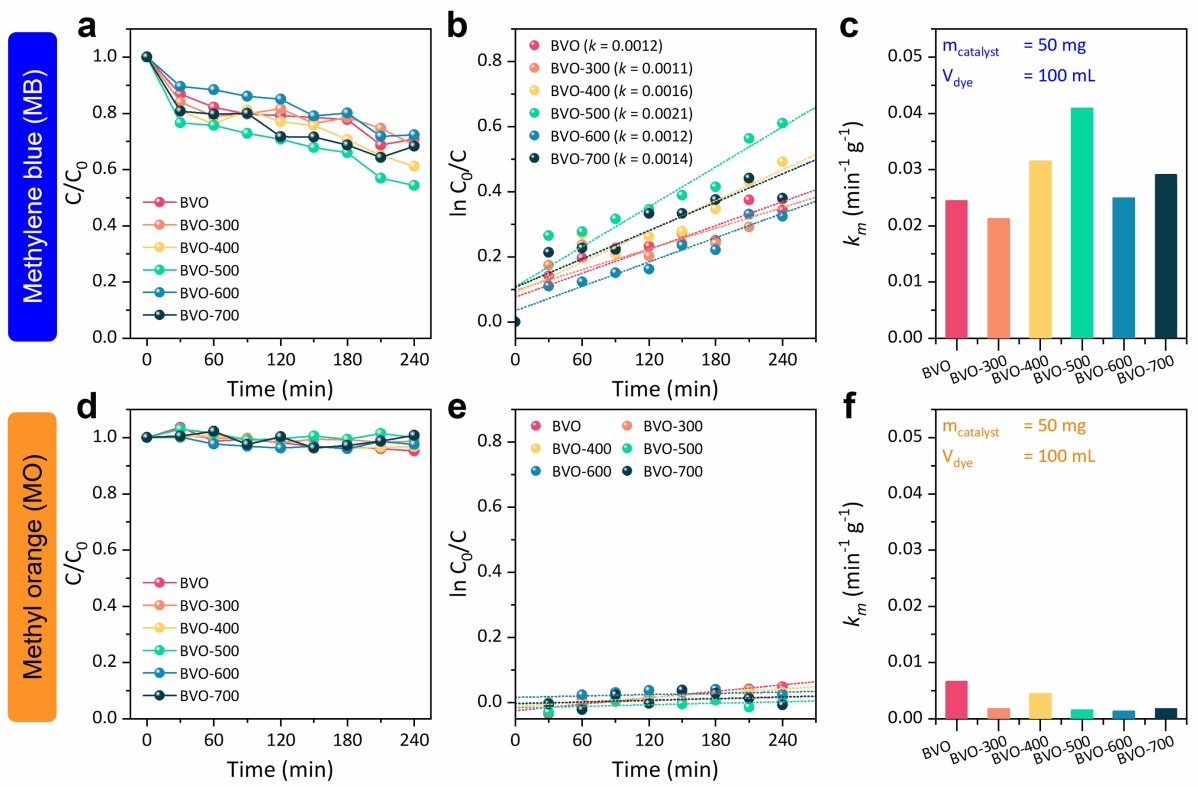

Figure 4. Photocatalytic removal of methylene blue (a to c) and methyl orange (d to f) under 254 nm irradiation. (a, d) C/C_0 against irradiation time. (b, e) $\ln(C_0/C)$ against irradiation time with linear fits, over 0 to 240 min for MB and 30 to 240 min for MO, and the apparent rate constants k (min^{-1}) for MB. (c, f) Mass-normalised rate constants k_m for 50 mg of catalyst in 100 mL of dye solution. MB was quantified from the integrated absorbance between 550 and 740 nm and MO from the absorbance at 464 nm.

which the chromophore is retained while methyl groups are removed [21], and its absence without catalyst suggests that this pathway is driven by the catalyst. Quantifying the residual dye at a fixed wavelength would therefore overstate its removal, and the integrated band area was used throughout.

Figure 4d shows the corresponding results for MO. With every sample, C/C_0 remains close to unity and lies between 0.95 and 1.01 after 240 min, and the mass-normalised rate constants stay below 0.007 min^{-1} g^{-1} (Figure 4e and 4f). $BiVO_4$ therefore does not degrade MO to a measurable extent under these conditions. The contrast with MB is consistent with the stronger interaction expected between the cationic dye and the catalyst surface, although the point of zero charge of these powders was not measured. For MB, the mass-normalised rate constant is highest for BVO-500 and lower on either side of it (Figure 4c), while BVO and BVO-300 remain close to the photolysis level. This pattern follows neither the monotonic lattice contraction nor the essentially constant band gap described above, so in this series the MB activity is not controlled by the refined structural or optical parameters. The decrease at 600 and 700 °C coincides with the sintering seen in Figure 1 and with the growth of the crystallite size in Figure 2h, which is consistent with a loss of accessible surface. For MO, none of the samples gives measurable removal (Figure 4d). These conclusions rest on single runs, so moderate differences between catalysts should not be over-interpreted.

4. CONCLUSIONS

$BiVO_4$ was prepared by a hydrothermal route and calcined between 300 and 700 °C, with the as-dried powder retained as a reference, so that calcination temperature was the only variable across the series. X-ray diffraction showed that the as-dried powder is already predominantly monoclinic clinobisvanite, and that its minor zircon-type fraction, below 2 wt%, disappears between 400 and 500 °C, so the monoclinic structure forms mainly during hydrothermal treatment rather than during calcination. Weak unindexed reflections appear only after calcination at 700 °C. Rietveld refinement of all six patterns gave a unit-cell volume that contracts monotonically from 310.179 to 309.750 $Å^3$. The contraction is anisotropic, with b shrinking by 0.081% against 0.035 and 0.023% for a and c, while the monoclinic angle γ shows no systematic trend. The lattice therefore densifies without a change in symmetry, which is consistent with the progressive removal of defects retained from the synthesis. The crystallite size remains between 96 and 103 nm up to 500 °C and then rises to 129 to 158 nm, and electron microscopy shows the particles changing from blocky and rod-like to rounded and joined by necks over the same interval. Diffuse reflectance shows a band gap of 2.49 to 2.54 eV that is essentially unchanged by calcination. Against a no-catalyst control, every sample leaves less MB after 240 min than photolysis alone, and BVO-500 gives the clearest enhancement, with an apparent rate constant about 2.6 times that of photolysis, whereas MO is not degraded. The MB activity follows neither the lattice contraction nor the band gap, so within the resolution of single runs it is not con-

© 2026 The Authors | CC-BY 4.0

trolled by the refined structural or optical parameters. Future work should measure the specific surface area of each sample, replicate the photocatalytic runs, and identify the reactive species by scavenger tests.

DATA AVAILABILITY

The datasets generated during and/or analyzed during the current study are available from the corresponding author on reasonable request.

CONFLICT OF INTEREST

The authors declare that there are no conflicts of interest.

AUTHOR CONTRIBUTIONS

Alex Triputra Lumban Tobing: Investigation, Writing – Original Draft. **Rima Nurfitria:** Investigation. **Rizky Aflaha:** Resources, Formal analysis. **Quratul Aini:** Investigation, Writing – Original Draft, Visualization, Writing – Review & Editing. All authors approved the final manuscript.

FUNDING

This work receives no funding.

REFERENCES

[1] Khan S, Noor T, Iqbal N, Yaqoob L. Photocatalytic Dye Degradation from Textile Wastewater: A Review. *ACS Omega*. 2024;9:21751-21767. doi:10.1021/acsomega.4c00887.

[2] Ramamurthy K, Priya PS, Murugan R, Arockiaraj J. Hues of risk: investigating genotoxicity and environmental impacts of azo textile dyes. *Environmental Science and Pollution Research*. 2024;31:33190-33211. doi:10.1007/s11356-024-33444-1.

[3] Zou Q, Wang B, Gao B, Jiang T, Feng Q, Chen M, Zhang J, Zhang X. Roles and mechanisms of carbonaceous materials in advanced oxidation coupling processes for degradation organic pollutants in wastewater: a review. *Biochar*. 2023;5:86. doi:10.1007/s42773-023-00285-z.

[4] Hama Aziz KH, Mustafa FS, Karim MAH, Hama S. Pharmaceutical pollution in the aquatic environment: advanced oxidation processes as efficient treatment approaches: a review. *Mater. Adv.* 2025;6:3433-3454. doi:10.1039/D4MA01122H.

[5] Rayaroth MP, Boczkaj G, Aubry O, Aravind UK, Aravindakumar CT. Advanced Oxidation Processes for Degradation of Water Pollutants—Ambivalent Impact of Carbonate Species: A Review. *Water (Basel)*. 2023;15:1615. doi:10.3390/w15081615.

[6] Kocijan M, Vukšić M, Kurtjak M, Ćurković L, Vengust D, Podlogar M. TiO_2-Based Heterostructure Containing g-C_3N_4 for an Effective Photocatalytic Treatment of a Textile Dye. *Catalysts*. 2022;12:1554. doi:10.3390/catal12121554.

[7] Chen SH, Jiang YS, Lin H. Easy Synthesis of $BiVO_4$ for Photocatalytic Overall Water Splitting. *ACS Omega*. 2020;5:8927-8933. doi:10.1021/acsomega.0c00699.

[8] Kurnia NR, Amanda T, Nurfitria R, Aflaha R, Widakdo J, Rianjanu A. Development and materials characterization of hydrothermally grown niobium-doped $BiVO_4$ for ciprofloxacin and methylene blue degradation. *Greensusmater*. 2025;2:55-61. doi:10.62755/greensusmater.2025.2.2.55-61.

[9] Tokunaga S, Kato H, Kudo A. Selective Preparation of Monoclinic and Tetragonal $BiVO_4$ with Scheelite Structure and Their Photocatalytic Properties. *Chemistry of Materials*. 2001;13:4624-4628. doi:10.1021/cm0103390.

[10] Walsh A, Yan Y, Huda MN, Al-Jassim MM, Wei SH. Band Edge Electronic Structure of $BiVO_4$: Elucidating the Role of the Bi s and V d Orbitals. *Chemistry of Materials*. 2009;21:547-551. doi:10.1021/cm802894z.

[11] Aguirre-Cortes JM, Moral-Rodríguez AI, Bailón-García E, Carrasco-Marín F, Pérez-Cadenas AF. $BiVO_4$-Based Photocatalysts for the Degradation of Antibiotics in Wastewater: Calcination Role after Solvothermal Synthesis. *Catalysts*. 2024;14:474. doi:10.3390/catal14080474.

[12] Qi Y, Wang M, Zhang Y, Zhu T. Effect of calcination temperature on the structure and photocatalytic performance of $BiVO_4$ prepared via an improved solution combustion method. *Micro Nano Lett*. 2018;13:1017-1020. doi:10.1049/mnl.2017.0564.

[13] Rianjanu A, Nuraeni R, Aflaha R, Khamidy NI, Triyana K, Taher T. Effect of calcination temperature on the performance of hydrothermally grown cerium dioxide (CeO_2) nanorods for the removal of Congo red dyes. *Greensusmater*. 2024;1. doi:10.62755/greensusmater.2024.1.1.9-14.

[14] Cai Y, Yang X, Li Y, Ling R, Sun G. Preparation and effects of calcining temperature and pH on the photocatalytic activity of $BiVO_4$ microcrystal for degrading methylene blue. *Ionics (Kiel)*. 2024;30:2333-2344. doi:10.1007/s11581-024-05407-6.

[15] Lotfi S, El Ouardi M, Arab M, Assani A, BaQais A, Haspel H, Kónya Z, Ait Ahsaine H. Polycrystalline $BiVO_4$ visible-light photocatalytic activity: Rietveld refinement, microstructural, vibrational, and photocatalytic properties. *Oxford Open Materials Science*. 2025;5. doi:10.1093/oxfmat/itaf005.

[16] Doebelin N, Kleeberg R. *Profex*: a graphical user interface for the Rietveld refinement program *BGMN*. *J. Appl. Crystallogr.* 2015;48:1573-1580. doi:10.1107/S1600576715014685.

[17] Mullens BG, Marlton FP, Nicholas MK, Permana AJ, Brand HEA, Maynard-Casely HE, Chater PA, Kennedy BJ. Intercalated Water Drives Anomalous Thermal Expansion in the Tetragonal Zircon Structured Bismuth Vanadate $BiVO_4$ Photocatalyst. *Chem. Asian J.* 2024;19. doi:10.1002/asia.202400408.

[18] Cooper JK, Gul S, Toma FM, Chen L, Liu YS, Guo J, Ager JW, Yano J, Sharp ID. Indirect Bandgap and Optical Properties of Monoclinic Bismuth Vanadate. *The Journal of Physical Chemistry C*. 2015;119:2969-2974. doi:10.1021/jp512169w.

[19] Khan MGI, Nurfitria R, Anggraini T, Aini Q, Hanifah IR, Nurfani E, Aflaha R, Triyana K, Taher T, Rianjanu A. Hydrothermal synthesis of CeO_2/ZnO heterojunctions for effective photocatalytic degradation of organic pollutants. *Materials Science and Engineering: B*. 2025;322:118630. doi:10.1016/j.mseb.2025.118630.

[20] Rianjanu A, Aini Q, Hanif R, Tambun SA, Triyadi D, Aflaha R, Yulianto N, Yudistira HT, Herbani Y, Taher T, Wasisto HS. Influence of temperature and reaction time on photocatalytic performance of $BaTiO_3$ nanoparticles for organic pollutant degradation in aqueous environment. *Surfaces and Interfaces*. 2025;70:106875. doi:10.1016/j.surfin.2025.106875.

[21] Zhang T, Oyama T, Aoshima A, Hidaka H, Zhao J, Serpone N. Photooxidative N-demethylation of methylene blue in aqueous TiO_2 dispersions under UV irradiation. *J. Photochem. Photobiol. A Chem.* 2001;140:163-172. doi:10.1016/S1010-6030(01)00398-7.

© 2026 The Authors | CC-BY 4.0